Magnetic Properties of Mixed Triangle-Based Ladder Magnets ($(C_1TET\text{-}TTF)(FeBr_4)_{1-x}(FeCl_4)_x$ (C_1TET-TTF: 4,5-Ethylenedithio-4′,5′-bis(methylthio)tetrathiafulvalene)

Masaya Enomoto,* Akira Miyazaki, and Toshiaki Enoki*

Department of Chemistry, Graduate School of Science and Engineering, Tokyo Institute of Technology,
Ookayama 2-12-1, Meguro-ku, Tokyo 152-8551

(Received September 5, 2000)

Isostructural magnets (C_1TET-TTF)FeX_4 (X = Br, Cl) are featured with a triangle-based ladder lattice comprised of an Fe^{3+} zigzag chain where a donor dimer bridges between next nearest neighboring Fe^{3+} sites. The $FeCl_4^-$ salt is an antiferromagnet with its easy axis tilted from the ladder sheet, the $FeBr_4^-$ salt shows weak ferromagnetism, with the easy axis of its antiferromagnetic behavior lying on the sheet. We investigate the magnetic properties of mixed crystal (C_1TET-TTF)$(FeBr_4)_{1-x}(FeCl_4)_x$ in order to reveal the origin of the differences in magnetism. The strengths of the exchange interactions varying with x can be understood on the basis of the inter-anion/donor atomic contact lengths in the crystal. Weak ferromagnetism survives with its easy axis tilted from the sheet in the concentration region $x \approx 0.2$. Then weak ferromagnetism disappears above $x \geq 0.42$. In the high concentration range $x \sim 0.4$–0.8, the ordered state deviates from an ordinary antiferromagnet, due to the competition between two constituent exchange interactions. However, the possibility of a spiral spin which configuration theory predicts is not conclusive. The magnetic anisotropy, whose direction varies depending on x, is a consequence of the competition between the dipole-dipole interaction and the single-ion anisotropy.

TTF-type donor molecules have been known to form charge transfer complexes or radical ion salts, where the large variety of properties in electron transport and magnetism is a result of the manner of molecular arrangement, the composition ratio, charge transfer ratio, and other factors.[1–5] Because these donors are generally planar-shaped molecules, they tend to form face-to-face and/or side-by-side arrangements, where inter-molecular contacts give electron conduction pathways, resulting in metallic state and even superconducting state in many cases. From the aspect of magnetism, these contacts also contribute to exchange interaction paths between magnetic moments. In this connection, the introduction of localized spins of *d*-electrons into TTF-type charge transfer complexes adds an important aspect in magnetism. The interplay between π-electrons in TTF molecules and *d*-electrons in counter anions produces a variety of types of magnetism: ferromagnetism, weak ferromagnetism, helical magnetism, etc.[4–10] In cases that complexes become metallic, the combination of π- and *d*-electrons contributes to the formation of metal-magnets at molecular levels,[4–10] which are reminiscent of *s*-*d* systems in ordinary metal magnets such as iron. An important advantage of TTF type charge transfer complexes in the development of molecular magnets is the easiness and controllability in the modification of magnetic structures by substitution of component atoms or functional groups. Actually, it is rather easy to introduce substitutional groups to the place which we desire in a donor molecule, and each substitution gives rise to distinct changes of magnetic properties.

In the present study, we employ C_1TET-TTF (4,5-ethylenedithio-4′,5′-bis(methylthio)tetrathiafulvalene: 2-[4,5-bis(methylthio)-1,3-dithiol-2-ylidine]-5,6-dihydro[1,3]dithiolo[4,5-*b*]1,4-dithiin) as a donor molecule (Fig. 1a) and FeX_4^- (X = Br, Cl) as a counter anion, where the localized magnetic moments of Fe^{3+} ($S = 5/2$) ions are incorporated into the π-electron network of C_1TET-TTF. The employment of C_1TET-TTF gives a feature of multi-channel exchange interactions associated with π-electrons. Namely, this donor molecule can mediate interactions along both short side and long side of the molecule, reflecting its specific shape with two different types of constituent parts.[11,12] The ethylenedithio group, such BEDT-TTF, prefers interaction along the short side of the molecule,[13] while the methylthio groups, such as TTM-TTF, lead to interactions along the long side.[14,15] According to the previous work about (C_1TET-TTF)$FeBr_4$,[16] Fe^{3+} spins are networked as a triangle-based ladder lattice, with the aid of the π-electron-mediated super exchange paths. Interestingly, our recent works[17] revealed a remarkable difference in magnetism between isostructural (C_1TET-TTF)$FeBr_4$ and (C_1TET-TTF)$FeCl_4$, which might be associated with differences in the strengths of exchange interactions and magnetic anisotropy; that is, the appearance of canted spin configuration and some difference in the directions of spin-easy axis. Triangle-based ladder spin system is one of interesting targets in both experimental and theoretical studies of magnetism from the point of the spin-gap formation.[18,19] However, a comprehensive understanding of the system remains unclear, especially for $S = 5/2$. Therefore, the systematic investigation of mixed crystals (C_1TET-TTF)$(FeBr_4)_{1-x}(FeCl_4)_x$

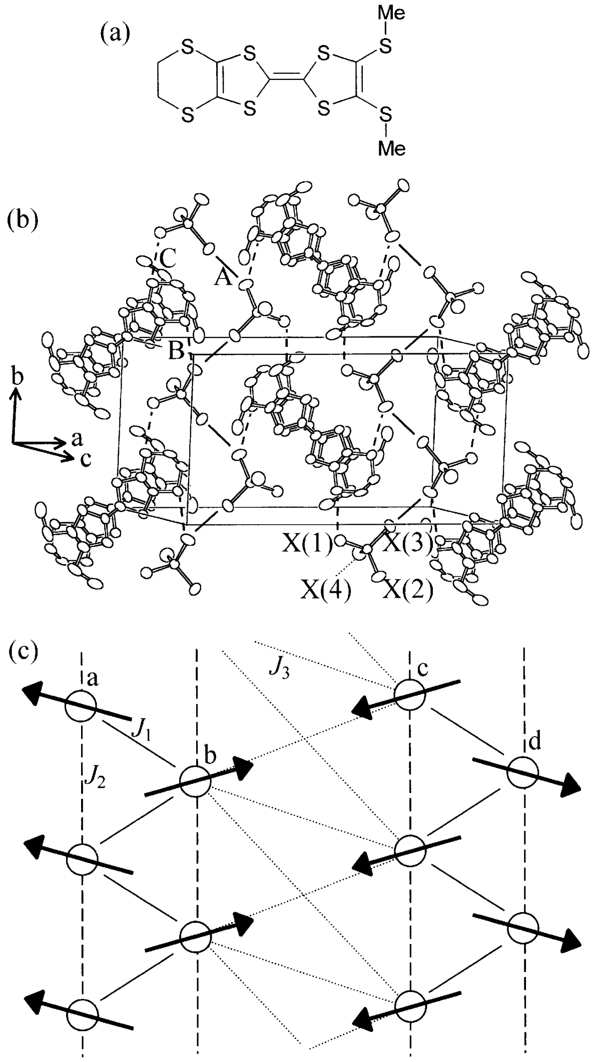

Fig. 1. (a) Molecular structure of C_1TET-TTF. (b) The crystal structure of (C_1TET-TTF)$(FeBr_4)_{1-x}(FeCl_4)_x$. There are close contacts between two halogen atoms (A) of adjacent FeX_4^- anions and those of halogen-sulfur atoms (B, C) between FeX_4^- and C_1TET-TTF donor. (c) The schematic model of exchange path network for triangle-based spin ladder system (C_1TET-TTF)FeX_4^-. Solid, dashed and dotted lines represent super-exchange paths for J_1, J_2 and J_3 respectively, which correspond to paths Fe–X–X–Fe, Fe–X–D–X–Fe and Fe–X–(D)$_2$–X–Fe, where D is donor. a, b, c and d denote sublattices constituting the unit cell of the magnetic lattice. The spin arrangement depicted in the figure corresponds to that for $x = 0$.

($0 \leq x \leq 1$) is expected to widen the perspective in the triangle-based ladder systems with $S = 5/2$, at the point where it can provide information about how the magnetic structure varies by changing a magnetic parameter such as exchange interaction or magnetic anisotropy.

In the present paper, we report the crystal structure and the magnetism of the mixed crystals in order to reveal the correlation between the crystal structure and the magnetic structure in relation to the magnetism of spin-ladder systems.

Experimental

The donor molecule, C_1TET-TTF was prepared according to the previous reports.[20] Single crystals of (C_1TET-TTF)$FeBr_4$, (C_1TET-TTF)$FeCl_4$ and mixed crystals (C_1TET-TTF) $(FeBr_4)_{1-x}(FeCl_4)_x$, were obtained by a galvanostatic (I = 0.5–2.0 μA) anodic oxidation of C_1TET-TTF (5 mg), using 50 mg of supporting electrolyte that consisted of mixtures of n-Bu_4NFeBr_4 and n-Bu_4NFeCl_4, and 15 cm^3 of ethanol distilled on Mg as a solvent. The typical sample size was $1 \times 0.2 \times 0.05$ mm^3 (corresponding to the c-, b- and a^*-axes, respectively) for all of these samples. Composition ratios of the obtained mixed crystals were determined from energy dispersive method in X-ray spectroscopy (EDX). We obtained eight compositions, that is, x = 0, 0.18, 0.22, 0.42, 0.56, 0.74, 0.89 and 1.0, using n-Bu_4NFeCl_4/{n-Bu_4NFeBr_4 + n-Bu_4NFeCl_4} = 0, 0.02, 0.05, 0.10, 0.15, 0.60, 0.80 and 1.0 in the starting solutions, respectively. The crystal structures were determined with a single crystal X-ray diffraction method using a Rigaku AFC-7 four-circle diffractometer at room temperature. The reflection data were collected in the range of 2θ = 5 to 55°, and the absorption effect was corrected empirically (ψ-scan method). The reflections that satisfy $|F_o|^2 > 4\sigma(|F_o|^2)$ were used for further analyses. The structures were solved with the direct methods using SHELXS-97,[21] then refined with the full-matrix least-squares method using SHELXL-97.[22] We refined crystal structures of mixed salts by using the concentration ratio of Br to Cl in the electron distribution function as an adjustable parameter. The coordinates of hydrogen atoms were calculated geometrically. The final atomic coordinates, the thermal parameters, complete bond distances and angles, and the lists of the observed and calculated structural factors are deposited as Document No. 74017 at the Office of the Editor of Bull. Chem. Soc. Jpn. Crystallographic data have deposited at the CCDC, 12 Union Road, Cambridge CB2 1EZ, UK and copies can be obtained on request, free of charge, by quoting the publication citationand the deposition numbers 156258–156266.

The magnetic susceptibilities and magnetization were measured using a Quantum-Design MPMS-5 SQUID magnetometer up to a field of 5T in the temperature range 1.8–300 K. Fifty to 100 single crystals (ca.0.5 mg) with their crystal axes aligned in the same direction were attached to the interior wall of a plastic straw by Apiezon N grease. The magnetic susceptibilities and magnetizations were obtained after the Pascal diamagnetic core contribution (χ_{dia}) was subtracted from the observed data. The values of χ_{dia} are estimated at -3.61×10^{-4} emu mol^{-1} and -3.21×10^{-4} emu mol^{-1} for x = 0 and 1, respectively. In the mixed crystals, χ_{dia} was obtained by the interpolation between the values for x = 0 and 1.

Results

All of the obtained salts have 1 : 1 donor-to-anion stoichiometry and are isomorphous to each other, regardless of the $FeBr_4^-/FeCl_4^-$ composition ratio. Table 1 summarizes the lattice parameters and final reliability factors in the crystal structure analyses. The atomic coordinates with thermal parameters for x = 0 and 1 are summarized in Tables 2a and 2b, respectively. From the refinement of the X-ray crystal structure data in the mixed salts, the ratio of x is estimated as 0.14, 0.18, 0.33, 0.44, 0.70 and 0.86, which correspond to x = 0.18, 0.22, 0.42, 0.56, 0.74 and 0.89 in the EDX data, respectively. Although the

Table 1. The Lattice Parameters for $(C_1TET\text{-}TTF)(FeBr_4)_{1-x}(FeCl_4)_x$

x	0	0.18	0.22	0.42	0.56	0.74	0.89	1
Space Group	$C2/c$	$C2/c$	$C2/c$	$C2/c$	$C2/c$	$C2/c$	$C2/c$	$C2/c$
a/Å	25.900(11)	26.139(4)	26.165(5)	26.300(8)	26.354(6)	26.400(9)	26.400(10)	26.414(3)
b/Å	12.184(4)	12.1096(9)	12.0898(12)	12.0124(17)	11.9663(13)	11.870(3)	11.815(3)	11.777(2)
c/Å	14.348(5)	14.2774(14)	14.265(3)	14.181(3)	14.147(3)	14.080(5)	14.052(5)	14.026(3)
β/°	99.54(3)	100.408(10)	100.547(15)	101.507(18)	102.016(16)	103.04(3)	103.52(3)	103.908(14)
V/Å^3	4465(3)	4444.9(9)	4436.3(13)	4390.1(17)	4363.6(14)	4299(2)	4261(2)	4235.5(14)
Z	8	8	8	8	8	8	8	8
No. of observed reflections ($\lvert F_o\rvert^2 > 4\sigma(\lvert F_o\rvert^2)$)	2096	2088	2153	2295	1862	2429	2500	3574
R	0.0855	0.0417	0.0501	0.0436	0.0491	0.0452	0.0405	0.0509

Table 2a. Atomic Parameters of $(C_1TET\text{-}TTF)FeBr_4$, with the Estimated Standard Deviations in the Parentheses

Atom	x	y	z	U_{eq}/Å^2
Fe1	0.34245(10)	0.18217(19)	0.35328(18)	0.0564(7)
Br1	0.42967(9)	0.12967(18)	0.3528(2)	0.0917(9)
Br2	0.32419(11)	0.33474(17)	0.25833(17)	0.0894(8)
Br3	0.28619(9)	0.04008(19)	0.29747(19)	0.0948(9)
Br4	0.33244(11)	0.2202(2)	0.50833(16)	0.0959(9)
S1	0.04966(17)	−0.0222(3)	0.1604(3)	0.0474(10)
S2	−0.02210(17)	0.1572(3)	0.0934(3)	0.0526(11)
S3	−0.04562(19)	−0.1955(4)	0.0965(3)	0.0583(12)
S4	−0.11370(17)	−0.0116(4)	0.0304(3)	0.0566(12)
S5	0.13829(19)	0.1198(4)	0.2385(3)	0.0585(12)
S6	0.0511(2)	0.3353(3)	0.1564(4)	0.0649(13)
S7	−0.1325(3)	−0.3599(5)	0.0434(5)	0.098(2)
S8	−0.2070(2)	−0.1572(6)	−0.0283(4)	0.093(2)
C1	−0.0122(6)	0.0193(12)	0.1079(11)	0.046(4)
C2	−0.0523(6)	−0.0563(13)	0.0828(10)	0.041(4)
C3	0.0731(6)	0.1113(12)	0.1814(10)	0.042(4)
C4	0.0402(7)	0.1937(13)	0.1500(12)	0.052(4)
C5	−0.1102(8)	−0.2259(16)	0.0485(14)	0.069(5)
C6	−0.1421(7)	−0.1387(16)	0.0187(12)	0.058(5)
C7	0.1502(8)	0.2644(13)	0.2294(14)	0.066(5)
C8	0.1075(7)	0.3389(11)	0.2461(12)	0.058(5)
C9	−0.0748(11)	−0.4381(17)	0.0856(16)	0.102(9)
C10	−0.2304(9)	−0.017(2)	−0.036(2)	0.122(10)
H7A	0.1812	0.2827	0.2743	0.080
H7B	0.1579	0.2790	0.1667	0.080
H8A	0.1209	0.4134	0.2514	0.069
H8B	0.0971	0.3198	0.3060	0.069
H9A	−0.0832	−0.5148	0.0830	0.153
H9B	−0.0615	−0.4176	0.1498	0.153
H9C	−0.0487	−0.4236	0.0468	0.153
H10A	−0.2670	−0.0167	−0.0614	0.182
H10B	−0.2115	0.0242	−0.0757	0.182
H10C	−0.2251	0.0144	0.0264	0.182

Table 2b. Atomic Parameters of $(C_1TET\text{-}TTF)FeCl_4$, with the Estimated Standard Deviations in the Parentheses

Atom	x	y	z	U_{eq}/Å^2
Fe1	0.33910(2)	0.18826(5)	0.34628(5)	0.0521(2)
Cl1	0.41980(5)	0.13791(13)	0.34800(16)	0.0937(6)
Cl2	0.31925(7)	0.33951(13)	0.25694(14)	0.0914(5)
Cl3	0.28571(5)	0.05192(13)	0.28670(15)	0.0894(5)
Cl4	0.33447(13)	0.2256(3)	0.49547(14)	0.1369(9)
S1	0.05891(4)	−0.02410(8)	0.16445(7)	0.0410(2)
S2	−0.01627(4)	0.16002(9)	0.10377(8)	0.0464(2)
S3	−0.03552(4)	−0.20629(9)	0.10151(8)	0.0465(2)
S4	−0.10851(4)	−0.01980(9)	0.04030(8)	0.0474(3)
S5	0.14933(4)	0.12360(9)	0.23943(9)	0.0521(3)
S6	0.05794(5)	0.34537(9)	0.16631(10)	0.0584(3)
S7	−0.12058(5)	−0.38408(12)	0.05029(11)	0.0682(4)
S8	−0.20042(4)	−0.17872(12)	−0.01878(10)	0.0647(3)
C1	−0.00503(14)	0.0161(3)	0.1144(3)	0.0410(8)
C2	−0.04519(14)	−0.0623(3)	0.0882(3)	0.0407(8)
C3	0.08276(14)	0.1148(3)	0.1858(3)	0.0400(8)
C4	0.04786(15)	0.1996(3)	0.1579(3)	0.0411(8)
C5	−0.10025(15)	−0.2438(4)	0.0583(3)	0.0469(9)
C6	−0.13456(15)	−0.1547(4)	0.0291(3)	0.0470(9)
C7	0.16061(19)	0.2754(4)	0.2358(4)	0.0592(11)
C8	0.1182(2)	0.3480(4)	0.2586(4)	0.0627(12)
C9	−0.0608(2)	−0.4602(5)	0.0909(5)	0.0735(15)
C10	−0.2274(2)	−0.0407(6)	−0.0155(6)	0.0882(19)
H7A	0.1932	0.2932	0.2825	0.071
H7B	0.1646	0.2952	0.1709	0.071
H8A	0.1305	0.4258	0.2674	0.075
H8B	0.1116	0.3229	0.3204	0.075
H9A	−0.0679	−0.5403	0.0894	0.110
H9B	−0.0442	−0.4378	0.1568	0.110
H9C	−0.0382	−0.4436	0.0484	0.110
H10A	−0.2645	−0.044	−0.0410	0.132
H10B	−0.2126	0.0102	−0.0549	0.132
H10C	−0.2198	−0.0138	0.0510	0.132

magnitudes of the values are a little small in the former, compared with those from EDX, the tendencies are consistent with each other. Therefore, we hereafter employ the composition ratio from EDX. The crystal structure of $(C_1TET\text{-}TTF)(FeBr_4)_{1-x}(FeCl_4)_x$ is shown in Fig. 1b. Donor molecules are dimerized in the head-to-tail configuration, while FeX_4^- anions form a one-dimensional zigzag chain extended along the b-axis through adjacent X(2)–X(3) atomic contacts (A in the figure).

There are two types of FeX_4^- tetrahedral anions in the crystal, which are oriented to different directions from each other. For both types, the Fe–X(1) bond is directed parallel to the (001) plane, where the angle between the two Fe–X(1) directions of adjacent FeX_4^- anions is estimated to be ca. 30° and the Fe–X(1) direction is tilted by 15° with respect to the a-axis. The Fe–X(4) bond is perpendicular to the $(10\bar{1})$ plane. Paying attention to the tetrahedral shape of FeX_4^-, the Fe–X(1) distance is about 1–2% longer than the other Fe–X distances irrespective of the concentration as shown in Fig. 2, although all the Fe–X distances decrease monotonically with increasing concentration x. The difference of the inter-atomic distance between Fe–X(2), Fe–X(3) and Fe–X(4) is meaningfully smaller than that between Fe–X(1) and Fe–X(i) ($i = 2, 3, 4$). Especially, there is a negligible difference between Fe–X(2) and Fe–X(3). Therefore, we can assume that the FeX_4^- tetrahedron is uniaxially distorted with respect to the Fe–X(1), despite the fact that a higher order distortion is present to some extent due to the difference between Fe–X(i) and Fe–X(j) ($i, j = 2, 3, 4$).

Donor dimers are stacked along the c-axis in the crossed configuration, suggesting a negligible strength of the orbital overlap between the donor molecule on the adjacent dimers. As for the side direction, there is no close contact between donor dimers since the anions between donor dimers separate them. In addition, no inter-anion halogen–halogen atomic contact along the c-axis is short enough to give an appreciable contribution. Eventually, we can neglect interaction along the c-axis.

A donor molecule bridges between two anions at every two sites in the same anion chain, with the aid of X–S contacts B and C, as shown in Fig. 1b. In this feature, Fe^{3+} magnetic anions form a triangle-based spin ladder lattice on the $(10\bar{1})$ plane, where short contacts X–X (A) and X–S (B and C) correspond to rungs and vertical pillars of the ladder lattice, respectively. Moreover, dimerized donor units mediate weak interaction between adjoining anion chains on the same plane. Thus, a ladder lattice is bridged to the adjacent ladder through the mediation of donor dimers. The X–X distance is 3.78 Å (Br–Br) for $x = 0$ and 3.66 Å (Cl–Cl) for $x = 1$, which are a little longer than the corresponding van der Waals distances d_{vdW}(Br–Br) = 3.70 Å and d_{vdW}(Cl–Cl) = 3.50 Å, respectively.[23] The X–S distances are 3.61–3.63 Å for $x = 0$ and 3.44–3.51 Å for $x = 1$ which are smaller than the corresponding van der Waals distances d_{vdW}(Br–S) = 3.65 Å and d_{vdW}(Cl–S) = 3.55 Å, respectively.[23] For us to compare the relative strengths of the atomic contacts in the whole concentration range $0 \le x \le 1$ more easily, the van der Waals distances corresponding to X–X and X–S, are estimated in the mixed salts by taking interpolation of the van der Waals distances between $x = 0$ and $x = 1$. Figure 3 shows the concentration dependence of the atomic contact distances X–X and X–S normalized with respect to the corresponding van der Waals distances. The normalized X–X distance shows an increasing trend with a concave curvature with increasing x. In contrast, the normalized X–S distances decrease linearly with increasing x. Considering the tendency that a smaller inter-atomic distance gives a larger interaction, we suggest that the inter-molecular interaction associated with the X–S atomic contact is more emphasized as concentration x increases, whereas that with the X–X atomic contact becomes smaller.

Figure 4 presents the temperature dependence of the magnetic susceptibility for the mixed crystal samples in a field of 1T applied parallel to the three crystallographic axes, a^*-, b- and c-axes. The susceptibilities obey the Curie–Weiss law with negative Weiss constants above ca. 30 K and deviate from the Curie–Weiss law below 30 K for all the salts, suggesting the presence of short-range order effects below this temperature. The Curie constants of about 4.6 emuK mol^{-1} are independent of concentration x, which correspond to $S = 5/2$ for Fe^{3+} ions. The π-electron spins on the donor molecules (1 spin/donor) therefore disappear by the formation of the singlet ground state in the dimered structure. Figure 5a shows the concentration de-

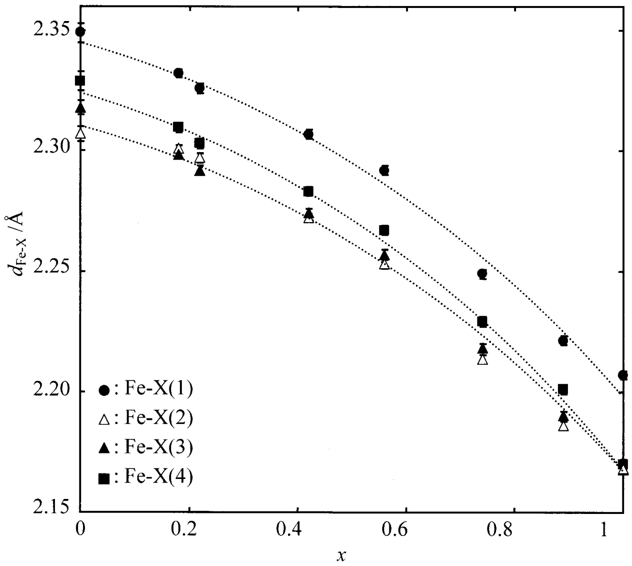

Fig. 2. The concentration dependence of the Fe–X distances in the FeX_4^- tetrahedron. Halogen atoms X(1), X(2), X(3) and X(4) and defined in Fig. 1. Fe–X(2) and Fe–X(3) are related to the contact between adjoining anions in the one dimensional zigzag chain. Experimental errors are within the sizes of symbols representing data points. Dotted lines are guides for the eyes .

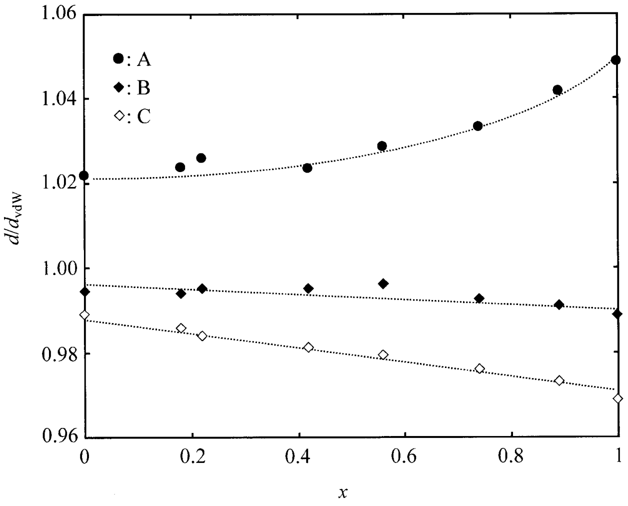

Fig. 3. The concentration dependence of the intermolecular atomic–contact distances between two halogen atoms X–X(A) and halogen-sulfur atoms X–S(B, C) , which are normalized with the corresponding van der Waals distances d_{vdW}. See Fig. 1 for the definitions of A, B and C. Dotted lines are guides for the eyes.

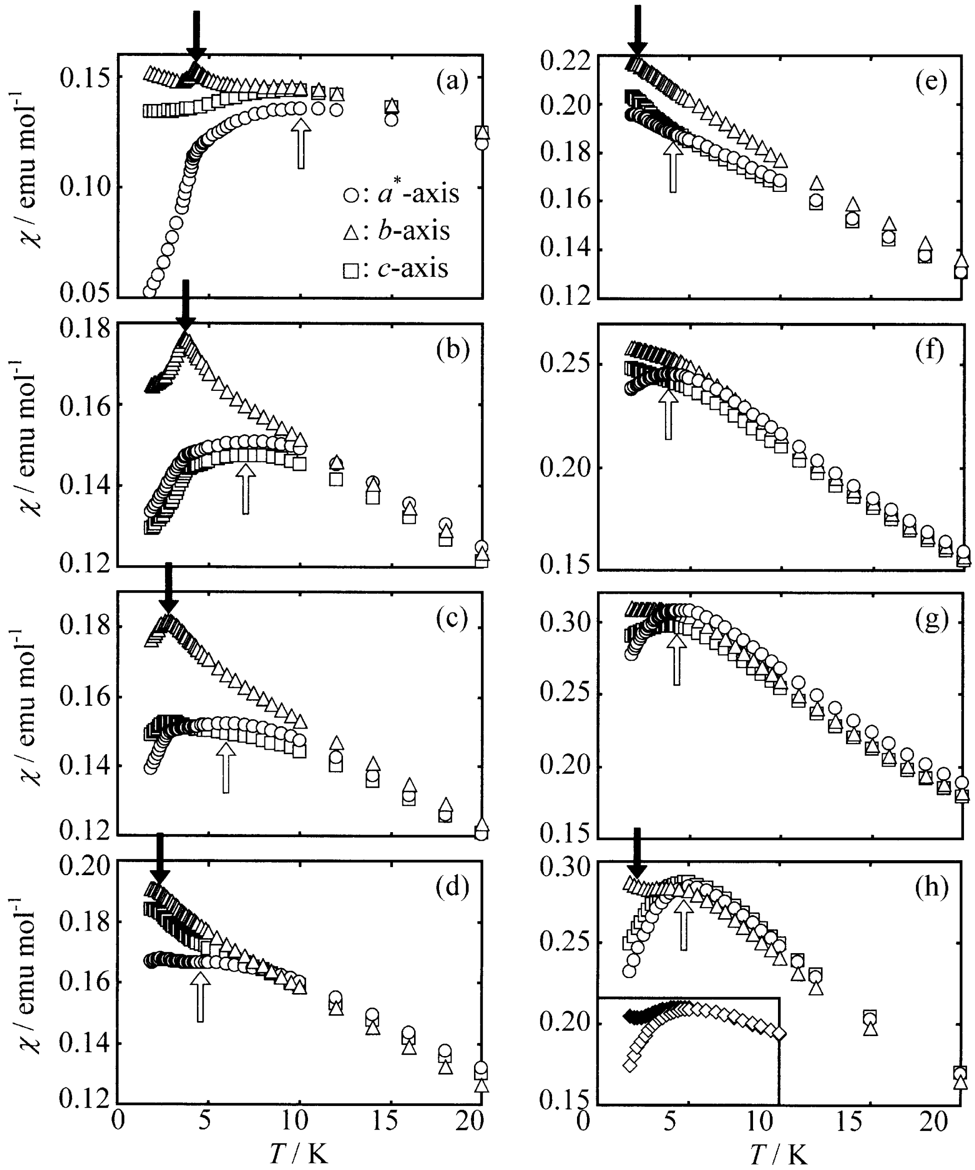

Fig. 4. The temperature dependence of the magnetic susceptibility of mixed magnets under $H = 1$ T applied in the three crystallographic axes (a^*, b, c) for (a) $x = 0$, (b) $x = 0.18$, (c) $x = 0.22$, (d) $x = 0.42$, (e) $x = 0.56$, (f) $x = 0.74$, (g) $x = 0.89$, and (h) $x = 1$. Open arrows represent the temperature (T_{max}) at which a broad hump appears in the a^*-axis, while closed arrows indicate the Néel temperature (T_{N}). Inset in (h) shows the susceptibility when the field is applied along the two intermediate directions 45° tilted from the a^*-axis in the ac-plane. The scale is arbitrary in the vertical axis.

pendence of the Weiss temperature. The Weiss temperature increases from −18 to −7 K, with increasing x from 0 to 1, showing a convex curvature in the $|\Theta|$ vs. x relation. Returning to Fig. 4, we see that there is a broad hump of short-range order in the susceptibility in the concentration range $0 \leq x \leq 0.22$, where the temperature of the hump (T_{max}) is lowered from 10 to 5.7 K as x increases from 0 to 0.22. In this concentration range, the mixed salts clearly show an antiferromagnetic transition, as evidenced by the presence of a sharp peak in the susceptibility at a low temperature for $H \parallel b$-axis. The Néel temperature (T_{N}) is lowered from 4.2 to 2.8 K as x increases from 0 to 0.22. An interesting behavior at these concentrations is the presence of a cusp around T_{N} when the field is applied along the b-axis, which is associated with the spin canting arrangement as discussed in the previous paper.[16] From the anisotropic behavior below T_{N}, the spin-easy axis for $x = 0$ is oriented in the a^*-axis direction, as shown in Fig. 4a. In contrast, the susceptibility tends to decrease with lowering the temperature for both $H \parallel a^*$-axis and $H \parallel c$-axis in the cases of $x = 0.18$ and 0.22 (Figs. 4b, 4c), suggesting that the easy axis lies in the ac-plane, although the decrement becomes rather small in comparison with that for $x = 0$. Actually, the susceptibility in the direction 45° tilted from the a^*-axis in the ac-plane has an easy axis trend, similar to that for $x = 1$ which will be shown later.

In the high concentration range $x \geq 0.42$, on the contrary, the trend in the susceptibility is changed from that at the low con-

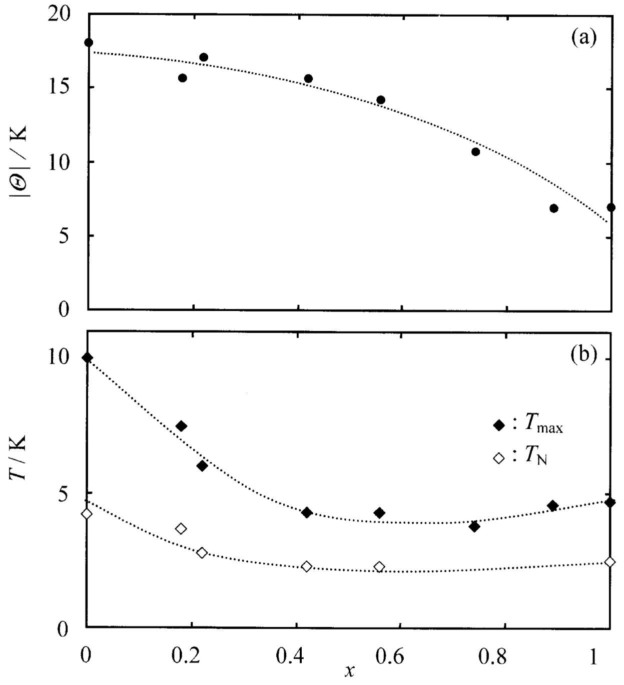

Fig. 5. The concentration dependence of the Weiss temperature Θ (a), the Néel temperature T_N (b) and the temperature of short-range order hump $T_{\max}$ (c). Dotted lines are guides for the eyes.

centrations. Figures 4d and 4e represent the susceptibility in x = 0.42 and 0.56, respectively. Interestingly, an anomaly appears at T_N = 2.3 K with no cusp of spin canting at these concentrations. For x = 0.42, a short-range order hump is observed around $T_{\max}$ = 4.4 K for $H \parallel a^*$-axis, while the susceptibility values in the other two directions still increase even below the hump as the temperature is lowered. The a^*-axis susceptibility shows a trend reminiscent of a spin-easy axis in spite of the absence of a decreasing trend below T_N. The anisotropy of the susceptibility becomes rather small for x = 0.56. A trace of a short range order hump emerges around $T_{\max}$ = 4.3 K, where the location of $T_{\max}$ is deduced as the point at which the absolute value of the derivative of the χ vs. T curve takes a minimum for $H \parallel a^*$-axis.

At x = 0.74 and 0.89, the a^*-axis behavior clearly shows a short range order hump at $T_{\max}$ 3.8 K and 4.5 K again as shown in Figs. 4f and 4g, respectively. For $H \parallel b$-axis and c-axis, the susceptibility still increases for x = 0.74 below $T_{\max}$ with the lowering of the temperature, although the slope becomes small. This behavior reminds us of x = 0.42 salt. On the other hand, x = 0.89 shows a decreasing tendency with lowering temperature below $T_{\max}$ for both a^*- and c-axes directions (This tendency is more pronounced for $H \parallel a^*$-axis). This behavior is like that for x = 1, as shown below. T_N is not easily determined from these results for x = 0.74 and 0.89, suggesting that the long range order state is most suppressed at these concentrations.

The susceptibility for the x = 1 has a broad maximum at $T_{\max}$ = 4.2 K. Although there is an anisotropy in the magnetic susceptibility below this temperature, this anomaly is not assigned to an antiferromagnetic transition, since the specific heat shows no magnetic transition anomaly at $T_{\max}$.[24] The c-axis susceptibility behaves very similarly to that of the a^*-axis as shown in Fig. 4h, showing that the spin-easy axis lies between the a^*- and the c-axes. The inset in Fig. 4h demonstrates that the easy axis is oriented toward the intermediate direction tilted by 45° from the a^*-axis in the ac-plane, while the hard axis behavior emerges in the direction perpendicular to the easy axis in the ac-plane. A spin-canting feature is also invisible for x = 1. Here, we determine T_N = 2.5 K as the point where the b-axis susceptibility take a minimum. At this temperature, the specific heat starts rising suddenly with lowering the temperature.

The x dependence of the Néel temperature T_N and temperature of short range order hump $T_{\max}$ are shown in Fig. 5b. Both T_N and $T_{\max}$ decrease monotonically with concave curvatures with increasing x, which are contrasted to the convex curvature in the Weiss temperature shown in Fig. 5a. Here, these concave curvatures are caused by different causal interactions between $T_{\max}$ and T_N: $T_{\max}$ reflects the short range ordered state, which is scaled by the mean value of the exchange field working on an individual Fe^{3+} spin in the mixed magnets. The concave curvature of $T_{\max}$ is suggestive of the enhancement in the compensation of exchange interactions in the intermediate concentration range. On the other hand, T_N is related to the stability of the long range ordered state, the enhanced randomness in the intermediate concentration range being considered to be responsible for the concave curvature in the T_N behavior.

Figure 6 shows the field dependence of the magnetization curves up to 5.5 T at 2 K in the external field along the a^*-, b- and c-axes. As shown in Fig. 6a, the magnetization curves for x = 0 shows a spin flop transition at H_{sf} = 2.3 T along the a^*-axis, whereas a weak ferromagnetism is induced above transition field H_{wf} = 2.3 T along the b-axis as discussed in the previous paper.[15] The magnetization for the c-axis is proportional to the applied field, showing the ordinary hard axis behavior (The presence of a small concave feature is the consequence of a small misalignment of the crystal in the experiment). The saturation field is estimated at H_C =17.7 T from the extrapolated value of the linear M vs. H line to the saturated magnetization (S = 5/2) for the b-axis, where the g-value (g = 2.01) is taken from ESR measurement and the straight line is obtained by the least-square-fitting of the initial slope of the M vs. H curve from the origin. The magnitude of an induced magnetization Δm_{wf} associated with the weak ferromagnetism is estimated at 0.17 μ_B from the step width at H_{wf} in the M vs. H plot in the b-axis.

From the Fig. 6b for x = 0.18 and 6c for x = 0.22, a careful inspection indicates that the M vs. H plots along the a^*- and c-axes have a downward bulge, which is regarded as a trace of a spin flop transition at H_{sf} = 2.0 T and 2.2 T for x = 0.18 and 0.22, respectively. Here, H_{sf} is estimated roughly by taking the field at which the magnetization deviates most from that expected by the straight line connecting the origin and the magnetization at the maximum field in the experiment. This can be more convincing in the estimation of H_{sf} than that estimated by taking the minimum in the derivative of the M vs. H curve,

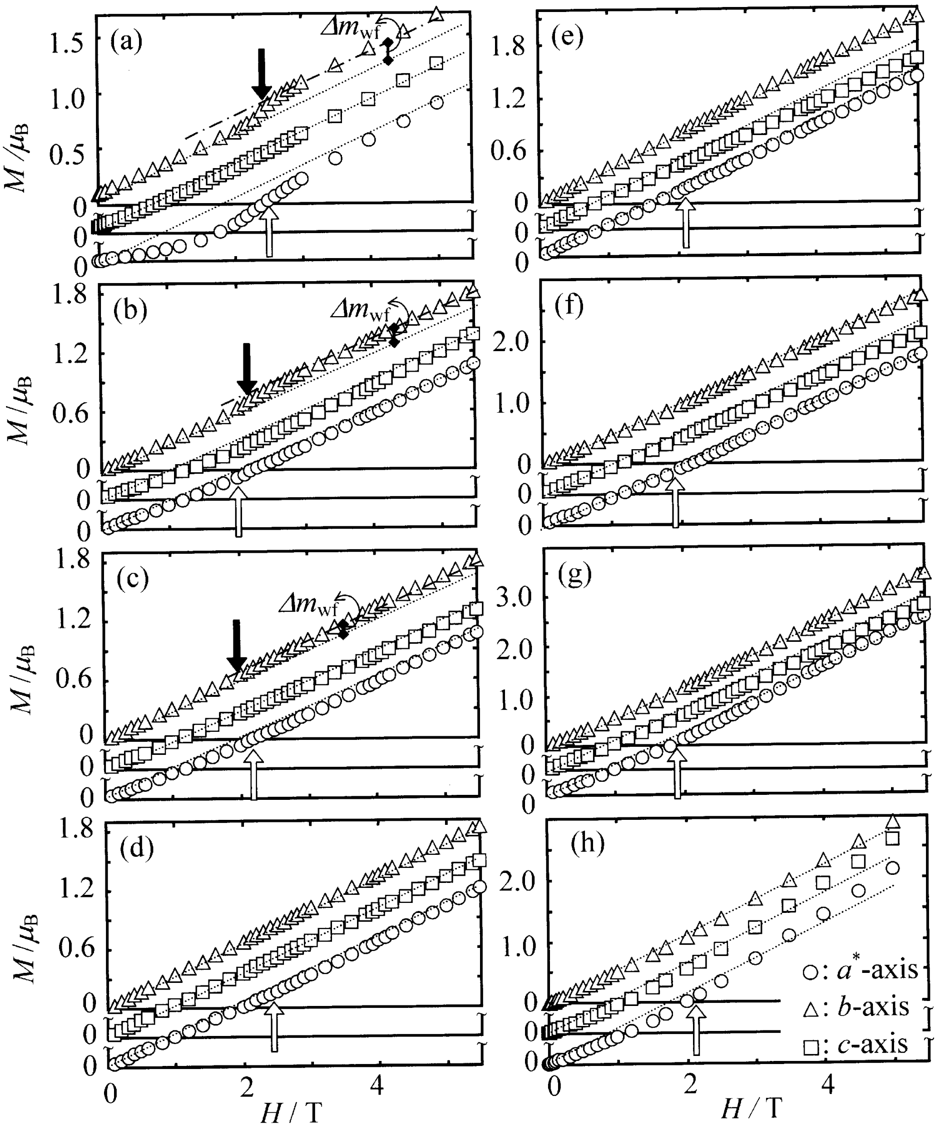

Fig. 6. The field dependence of the magnetization curves along the three crystallographic axes (a^*, b, c) at T = 2 K for (a) x = 0, (b) x = 0.18, (c) x = 0.22, (d) x = 0.42, (e) x = 0.56, (f) x = 0.74, (g) x = 0.89, and (h) x = 1. Dotted lines are drawn as straight lines representing an initial slope of the M vs. H curve from the origin for $H \parallel b$-axis. The same dotted lines are shown for comparison, also for $H \parallel a^*$-axis and c-axis. The dot-dash line in the high field range for $H \parallel b$-axis is the fitting line of the data, whose slope is the same to that of the dotted line. Δm_{wf} with a double arrow is the magnetization associated with the appearance of weak ferromagnetism. See text for estimatin of the spin flop field H_{sf}.

since the numerical derivative brings about more ambiguity in the estimation due to the experimental errors in the data. The same procedure is employed hereafter for the estimation of H_{sf}.

The magnetization behavior for $H \parallel a^*$-axis and c-axis is consistent with the similar behavior of the susceptibilities between the a^*- and c-axes, as mentioned before. Namely, the spin easy axis is directed to the direction intermediate between the a^*- and c-axes. The saturation fields are estimated as H_{C} = 16.9 T and 17.0 T for x = 0.18 and 0.22, respectively, using the same procedure as that for x = 0. In addition, in the b-axis, the magnetization curves for x = 0.18 and 0.22 show induced weak ferromagnetism developing at H_{wf} = 2.1 T and 1.9 T, respectively. The magnitudes of induced magnetization are estimated as H_{wf} = 0.13 μ_{B} and 0.08 μ_{B} for x = 0.18 and 0.22, respectively.

The magnetization data are shown for x = 0.42, 0.56, 0.74 and 0.89 in Figs. 6d–g. For all samples, the a^*-axis magnetization has a slightly downward bulge suggestive of a spin-flop transition, from which a spin flop field H_{sf} is estimated at H_{sf} = 2.4 T, 2.2 T, 1.9 T and 1.9 T for x = 0.42, 0.56, 0.74 and 0.89, respectively. In the b- and c-axes magnetization curves, there is no indication of anomaly. The saturation fields of these salts are estimated at H_{C} = 15.9 T, 14.0 T 10.2 T and 7.8 T for x = 0.42, 0.56, 0.74 and 0.89, respectively.

Finally, x = 1 shows a spin flop transition at H_{sf} = 2.1 T both for the a^*- and c-axes as shown in Fig. 6h. The concave curvature in the magnetization is more conspicuous than that of the other concentrations. This also suggests that the easy axis is oriented in the intermediate direction between these axes, consistent with the behavior of the susceptibility. The *M* vs. *H* curve of the *b*-axis is slightly concaved, indicating a trace of the spin-flop transition due to the misalignment of the crystal (Considering the shape of this crystal, we argue that the *b*-axis component is susceptible to *c*-axis).

The concentration dependence of H_C, H_{sf}, H_{wf} and Δm_{wf} is summarized in Fig. 7. From these results, H_C monotonically decreases with a convex curvature on the increase of *x*, which well corresponds to the trend of the Weiss temperature (Fig. 5a) representing the strength of the molecular field. The spin-flop transition field H_{sf} is almost independent of the concentration, while the values of H_{wf} and Δm_{wf} for the weak ferromagnetism decrease steeply as the concentration is elevated, the values disappear above $x \sim 0.22$.

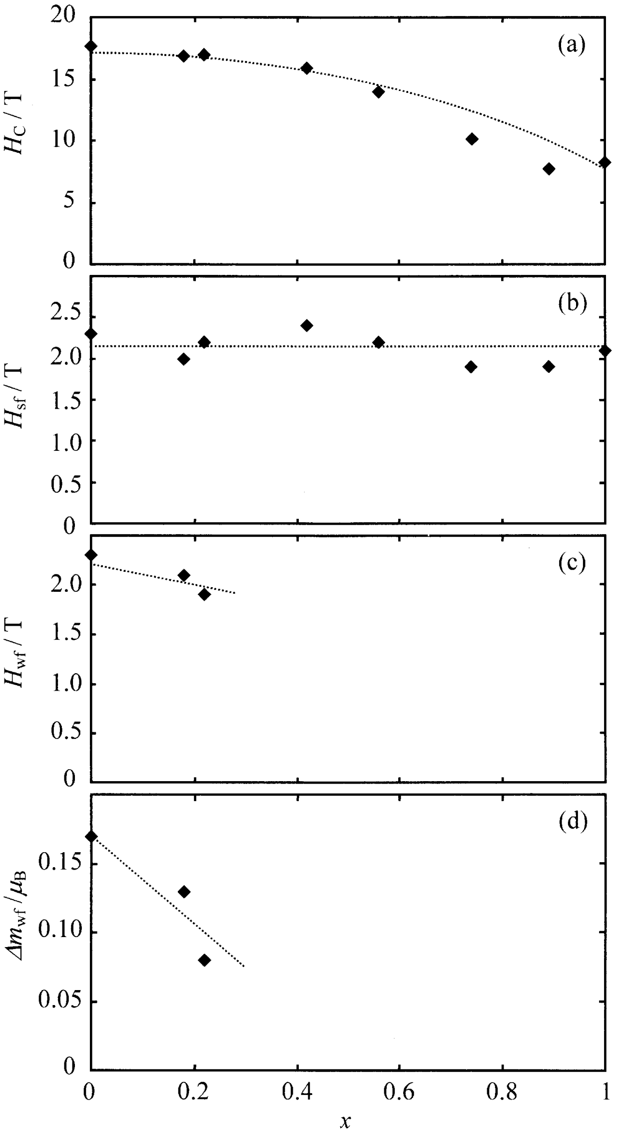

Fig. 7. The concentration dependence of (a) the saturation field H_C, (b) spin-flop field H_{sf}, (c) the weak ferromagnetic transition field H_{wf} and (d) the induced magnetization of weak ferromagnetism Δm_{wf}. Dotted lines are guides for the eyes.

Discussion

Firstly, we discuss the correlation between the crystal structure and the magnetic structure. The Fe^{3+} magnetic lattice can be treated on the basis of triangle-based ladder lattice on $(10\bar{1})$ plane, as shown in Fig. 1c. The variation of composition ratio *x* induces changes in the inter-molecular atomic distances, yielding the modification in strengths of exchange interactions associated with the inter-molecular atomic contacts. The super-exchange interaction network that is related to the three types of short contacts is modeled as shown in Fig. 1c with antiferromagnetic J_1 (Fe–X–X–Fe path), J_2 (Fe–X–(donor)–X–Fe path) and J_3 (Fe–X–(donor)$_2$–X–Fe path). The former two J_1 and J_2 contribute to the backbone of the spin ladder network, whereas the exchange path through donor dimer J_3 works to link weakly between adjacent ladders on the same plane. Here, using a molecular field treatment with the four-sublattice model[16] with sublattices a, b, c and d in Fig. 1c, we analyze the magnetic structures of the mixed magnets. The quantities related to the molecular field treatment *C*, Θ and T_{max} are treated in the same way as in the previous paper.[16] Figure 8a shows the

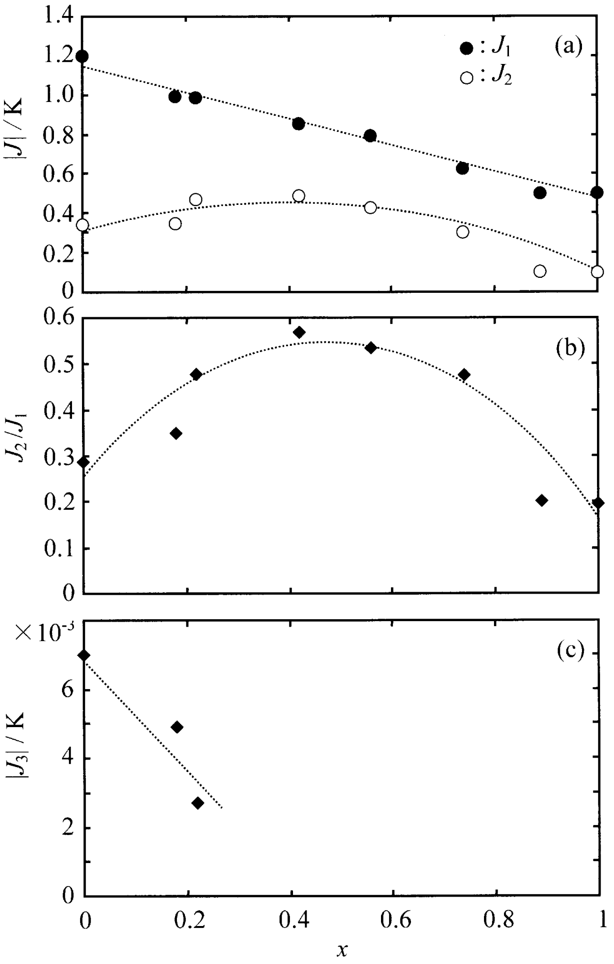

Fig. 8. The concentration dependence of exchange interactions J_1, J_2 and J_3. J_1, J_2 and J_3 are antiferromagnetic (< 0). Dotted lines are guides for the eyes.

concentration dependence of exchange interactions, $|J_1|$ and $|J_2|$. The strengths of J_1 and J_2 are in the range of 0.2–1.2 K. $|J_1|$ is larger than $|J_2|$ in the whole concentration range. $|J_1|$ decreases in proportion to concentration x, while $|J_2|$ is gently elevated up to $x = 0.42$, and then it decreases above the concentration after a broad maximum around $x \sim 0.4$. The monotonical decrease in the strength of J_1 can be explained in terms of the elongation of the normalized inter-anion X–X atomic contact upon the variation of x, taking into account that the normalized X–X atomic contact (A) shown in Fig. 3 increases monotonically with increasing x. The increasing trend in $|J_2|$ in the low x region is consistent with the monotonical decrease of the normalized value of atomic contacts B and C. Although the decrease in $|J_2|$ in the high x region seems to be inconsistent with the changes of the distance between halogen-sulfur atoms, a subtle change in the orbital overlap can contribute to this change.

Using the changes of these two exchange interactions, the ratio J_2/J_1 is obtained, as shown in Fig. 8b. From theoretical results, the triangle ladder systems in the classical limit ($S \rightarrow \infty$) have two types of ground states, depending on the J_2/J_1 ratio.[25,26] Namely, an antiferromagnetic ground state is stabilized in the range of $J_2/J_1 < 0.25$, while a spiral spin state appears for $J_2/J_1 > 0.25$ as a result of the competition between J_1 and J_2. According to the theory, the present magnetic system seems to be included in the spiral phase, except at $x = 0.89$ and 1, as evidenced in Fig. 8b.

For $x = 1$, an ordinary antiferromagnetic ordered state is stabilized, consistent with the theoretical prediction, where the spin-easy axis becomes oriented in the intermediate direction between a^*- and c-axes. The sample with $x = 0$ takes an antiferromagnetic arrangement with the spin-easy axis oriented along the a^*-axis in spite of $J_2/J_1 > 0.25$. This seems to contradict the theoretical prediction. However, a small difference in the J_2/J_1 value from that at the spiral magnet-antiferromagnet threshold is the consequence of the difference between the theoretical model and the actual system in the experiment.

For $x = 0.18$ and 0.22, there is no evidence of spiral behavior, in disagreement with the theory. Instead, an ordinary antiferromagnetic transition takes place in that region, the spin-easy axis being along the intermediate direction between the a^*- and c-axes, as can be clearly seen in Figs. 4b and 4c. There is no definite explanation for the disagreement between the theory and the experiment. But the role of the inter-ladder interaction J_3 can also give the difference between the experiment and the theory, although the strength is 2–3 orders of magnitudes smaller than the strengths of J_1 and J_2. Actually, the contribution of J_3 is large in this concentration range in comparison with the higher concentrations (see Fig. 8c), as will be discussed later in relation to the weak ferromagnetism.

The situation is not conclusive for $x = 0.42$ and 0.56, which have the J_2/J_1 values considerably larger than the value predicted at the antiferromagnet-to-spiral magnet transition. The concave curvature in the $T_{\max}$ vs. x plot (Fig. 5b), which tends to be opposed to the convex curvature in the $|\Theta|$ vs. x plot, clearly reveals that antiferromagnetic J_1 and J_2 compete oppositely, producing a serious compensation of exchange interactions, which makes the antiferromagnetic ordered state less stabilized in the intermediate concentration range. This becomes a favorable situation in stabilizing a spiral spin configuration. It should be noted that the magnetic anisotropy can be explained in terms of uniaxial features with respect to the a^*-axis, especially for $x = 0.42$, different from the behavior for the samples at the neighboring concentration $x \sim 0.22$ and $x = 1$. At the same time, the increasing trend of the susceptibility in all the directions with decreasing temperature in the vicinity of T_N suggests the absence of a unique axis for the orientation of spins in the ordered state, giving a possibility of a spiral spin configuration. In this concentration range, however, the long-range order is seriously suppressed by the randomness of the ligand atoms. Therefore, the features of the ordered state in addition to the direction of easy axis are rather obscure, different from the case in the neighboring concentration ranges which show ordinary antiferromagnetism.

The value $x = 0.74$ shows anisotropic features, with the a^*-axis as a favorable spin orientation. However, the anisotropy is rather small compared with that for $x = 0.22$, which has ordinary antiferromagnetic state, in addition to the small decrement of the a^*-axis susceptibility on the low temperature side of $T_{\max}$. The deviation of x from 0 or 1 brings about the randomness in the magnetic lattice. The degree of randomness increases as the deviation becomes larger. In this context, the sample with $x = 0.74$ should have a very similar degree of randomness to that with $x = 0.22$, since the deviation in the former is about the same to that in the latter. Therefore, the randomness is not considered to give a fatal effect in the diagnosis of the spin ordered state for $x = 0.74$, as it does not for $x = 0.22$. Eventually, the sample with $x = 0.74$ having a small anisotropy, whose exchange interaction ratio J_2/J_1 is in the range of spiral state from theoretical predictions, can be a candidate of spiral spin state in the triangle-based ladder system, although further investigation should confirm this. The sample with $x = 0.89$ tends to have an intermediate situation between $x = 0.74$ and $x = 1$.

We also extract information on the magnetic structure from the magnetization curves. The spin-flop field and the saturation field are related to the anisotropy field and the exchange field as expressed in the following equations; $H_{\mathrm{sf}} = \sqrt{H_A(2H_E - H_A)}$ and $H_C = 2H_E - H_A$, where H_A and H_E represent the anisotropy field and the exchange field, respectively. From these equations, H_A and H_E are calculated, as shown in Fig. 9. The exchange field H_E decreases with a convex curvature with increasing x. In contrast, the anisotropy field, H_A, tends to increase with a concave curvature with increasing x. Interestingly, the spin-easy axis is oriented to the a^*-axis for $x = 0$, it is along the intermediate direction between the a^*- and the c-axis for $x = 0.18$ and 0.22, and then $x = 0.42$–0.89 have roughly the a^*-axis uniaxial features. Finally, the easy axis becomes oriented along the intermediate direction. Consequently, with respect to the spin easy axis or magnetic anisotropy, there are four concentration regions with different spin easy axes; $x = 0$, 0.18–0.22, 0.42–0.89 and 1. This fact shows that the spin arrangement in the ordered state varies with complexity depend-

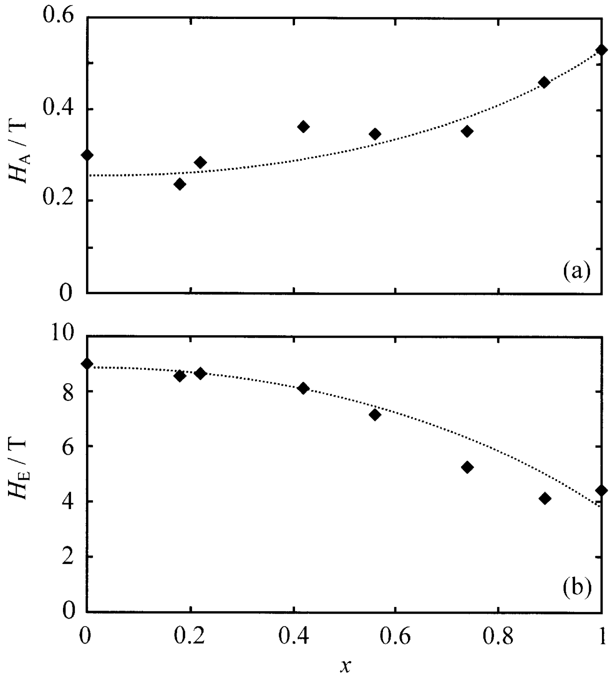

Fig. 9. The concentration dependence of anisotropic field H_A (a) and exchange field H_E (b). Dotted lines are guides for the eyes.

ing on the concentration, as partly discussed before in relation to the ordered state expected for the spin-ladder system. Here, the correlation between the direction of the easy axis and the anisotropy field should be consistently explained. There are two origins for the magnetic anisotropy: the dipolar anisotropy and the single-ion anisotropy. The dipolar anisotropy is calculated with the dipole–dipole interaction of an Fe^{3+} spin with the neighboring Fe^{3+} spins involved in the surrounding spherical region of 50 Å radius. From the arrangement of Fe^{3+} spins in the crystal, the dipole–dipole interaction is found to contribute to the anisotropy with the spin-easy axis oriented to the *c*-axis, which is perpendicular to the sheet of the spin-ladder network. The anisotropy field associated with the dipole-dipole interaction is estimated at 0.38 T irrespective of the composition ratio. In contrast, the experimental observation suggests that the spin-easy axis is tilted from this direction for all the samples with different concentrations. This deviation is considered to originate from the single-ion anisotropy of spin–orbit interaction origin. The larger deviation of the spin-easy axis for $x = 0$, which is rotated almost 90° from that expected from the dipole–dipole interaction, suggests a larger contribution of the single-ion anisotropy in comparison with the sample for $x = 1$ that prefers the intermediate direction between the a^*- and *c*-axes for the easy axis. There is a uniaxial anisotropy in the FeX_4^- tetrahedral anion associated with the low symmetry field with respect to the Fe–X(1) direction roughly parallel to the *a*-axis as we have discussed before. Therefore, taking into account that the easy axis is oriented along the a^*-axis for $x = 0$, we conclude that single-ion anisotropy plays a major role in the magnetic anisotropy. As x is elevated, the easy axis is rotated to the direction more favorable to the dipolar anisotropy suggesting less importance of the single-ion anisotropy. Because the anisotropic field H_A is composed of the dipolar anisotropy and the single-ion anisotropy, we can calculate the magnitude of the single-ion contribution, assuming that the direction of the H_A corresponds to the observed spin-easy axis direction. The single-ion anisotropy is estimated by subtracting the vector of the dipolar anisotropy field from the vector of the observed anisotropic field, where the direction of the single-ion anisotropy is scattered in the range of 10°–40° with respect to the Fe–X(1)direction, due to the limited accuracy of the experimental data. Figure 10 summarizes the result of this calculation. Here, it should be noted that two neighboring FeX_4^- anions give different anisotropy axes in the *ab*-plane, where the angle between the two anisotropy axes is estimated at ca. 30°. This also contributes to the limited accuracy in the estimation. The small magnitude of the single-ion anisotropy is in a reasonable range for the electronic state of the high spin d^5 configurations.[27] The roughly decreasing trend of the single-ion anisotropy with x suggests that the spin-orbit interaction associated with the Fe^{3+} *d* electronic state with an admixture of ligand halogen states is reduced by the substitution of Br ligands with Cl ligands having smaller spin–orbit interaction.

Next, we discuss the contribution of inter-ladder antiferromagnetic interaction J_3. According to a previous paper,[16] J_3 is relevant to the weak ferromagnetic transition, as given by the following relation, $6J_3SS = \Delta m_{wf}H_{wf}$. In the present case, the weak ferromagnetism is observed in the range up to $x = 0.22$. The calculated values of $|J_3|$ are shown in Fig. 8c as a function of concentration x. The strength of J_3 is in the range of 10^{-3} K, which is 2–3 orders of magnitudes smaller than the strengths of J_1 and J_2. $|J_3|$ decreases steeply as the concentration is elevated and it becomes less than the value range within our observation. From a viewpoint of the crystal structure, the normalized X–S distance and the overlap integral of donors in a dimer determine the strength of J_3. The result of the X-ray crystal analysis shows that the inter-ladder distance tends to be elongated

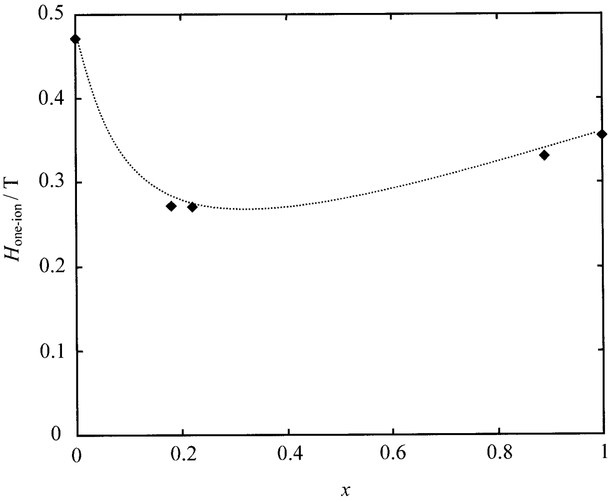

Fig. 10. The concentration dependence of the expected contribution of the single-ion anisotropy field. Data for $x = 0.42$–0.74 are omitted due to their inaccuracy. A dotted line is a guide for the eyes.

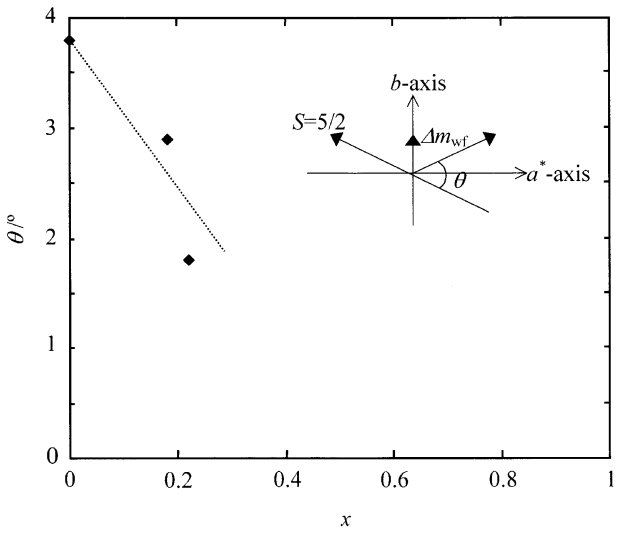

Fig. 11. The canting angle of the weak ferrornagnetic arrangement as a function of x. A dotted line is a guide for the eyes. Inset shows the canted spin configuration.

with increasing the concentration x; that is, the normalized direct distance between sites b and c in Fig. 1c is elongated by 3% when x goes from 0 to 1. Moreover, the overlap integral becomes smaller by 2% from $x = 0$ to $x = 1$ ($S = 3.83 \times 10^{-2}$ and 3.74×10^{-2} for $x = 0$ and 1, respectively). Therefore the steep decrease of $|J_3|$ can be well explained on the basis of the crystal structure.

Finally, we discuss weak ferromagnetism appearing in the low concentration regime. The induced magnetization $\Delta m_{\rm wf}$ is directly related to the canting angle θ, which is estimated as shown in Fig. 11. θ rapidly decreases from 3.8° to 1.8° with increasing x up to $x = 0.22$. One of the causes of this spin canting arrangement is also the single-ion anisotropy. As mentioned above, the single-ion anisotropy exists along the Fe–X(1) direction. There are two types of FeX_4^- anions whose Fe–X(1) directions take a mutual angle of ca. 30°, where the median lines between the two directions are directed to the a- and b-axes, as shown in Fig. 11. The canting angle ranging 3.8–1.8° is almost one order of magnitude smaller compared with the angle between the two Fe–X(1) directions. The cooperation of exchange interaction with the single-ion anisotropy can produce the observed spin canting configuration as the exchange interaction works to reduce the canting angle. Another candidate of the origin of the canting arrangement is the Dzyaloshinski–Moriya (D–M) interaction, judging from the absence of the inversion center between adjoining two anion spin sites. Applying this interaction to the present mixed crystal system, we interpret the decrease of canting angle as due to the decrease of the antisymmetric exchange interaction, D. The magnitude of D decreases with decreasing the exchange interaction J_1 and J_2. Here, we know that the exchange interaction of this mixed salt system decreases with increasing x. Eventually, the decrease of the exchange interactions is consistent with D–M interaction feature. Here, we have to note that the canting angle from the D–M interaction is so small as about 1°, in general. This is consistent with that observed in the experiments. The actual situation for the spin canting can be understood on the basis of a combination of the single-ion anisotropy and the D–M interaction. No weak ferromagnetism appears for $x = 0.42$ to 1. This is partly owing to the difference in the relative temperature at which the observation is carried out. The magnetization is observed at relatively higher temperatures for $x = 0.42$–1 with respect to the strengths of the exchange interactions. This makes the thermal agitation work at reducing effectively the canting angle. The decrease in the single-ion anisotropy with increasing x is also considered to cooperatively reduce the weak ferromagnetism.

Summary

We investigated the magnetic properties of isostructural Fe^{3+} ($S = 5/2$) mixed magnets of organic radical ion salts $(\text{C}_1\text{TET-TTF})(\text{FeBr}_4)_{1-x}(\text{FeCl}_4)_x$. The magnetic lattice is modeled with a triangle-based ladder lattice, from the crystal structure composed of one-dimensional anion zigzag chain and donor dimers, where donors contribute to super-exchange paths both for one of the spin ladder interactions and the inter-ladder interaction. The strengths of the intra-ladder interactions J_1, J_2 and the inter-ladder interaction J_3, all of which vary depending on concentration x, can be understood on the basis of the inter-anion/donor atomic contacts giving super-exchange paths. An antiferromagnetic transition takes place with its easy axis parallel to the plane of the ladder lattice for $x = 0$, in addition to the appearance of weak ferromagnetism. In the low concentration range, the easy axis is rotated to the intermediate direction between the a^*- and c-axes $x = 0.18$–0.22, with weak ferromagnetism surviving. In the middle concentration range, $x = 0.42$–0.74, the spin-easy axis becomes oriented along the a^*-axis, where a possibility of a spiral spin structure is not excluded as a plausible spin arrangement as theoretical prediction suggests. $x = 0.89$ indicates a anisotropic behavior, which remains during the process of changing its easy axis from frustrated state to ordinary anitiferromagnet. Finally, an ordinary antiferromagnetic state is stabilized at $x = 1$ where the spin-easy axis is again rotated to the intermediate direction.

This anomalous behavior in the changes of the spin-easy axis orientation is explained by a competition between the dipolar anisotropy and the single-ion anisotropy. The dipole–dipole interaction prefers the c-axis direction as the easy axis, whereas the single-ion anisotropy takes the Fe–X(1) direction roughly oriented to the a-axis direction. The canting angle in the weak ferromagnetic state is estimated at 3.8° for $x = 0$ and it steeply reduced as the concentration is elevated. Not only the Dzyaloshinski–Moriya interaction but also the single-ion anisotropy play a role in the spin canting arrangement.

The authors would like to express their sincere thanks to Profs. Y. Ajiro, H. Tanaka and Y. Kaizu for their fruitful discussions. M. E. was supported by Research Fellowships of the Japan Society for the Promotion of Science for Young Scientists. This work is partly supported by a Grant-in-Aid for Scientific

Research No. 12046231 from the Ministry of Education, Science, Sports and Culture.

References

1 D. Jérome, and H. Schulz, *Adv. Phys.*, **31**, 299 (1982).

2 T. Ishiguro and K. Yamaji, "Organic Superconductors," Springer-Verlag, Berlin (1990).

3 J. M. Williams, J. R. Ferraro, R. J. Thorn, K. D. Carlson, U. Geiser, H. H. Wang, A. M. Kini, and M. -H. Whangbo, "Organic Superconductors," Prentice Hall, New Jersey, (1992).

4 T. Enoki, J.-I. Yamaura, and A. Miyazaki, *Bull. Chem. Soc. Jpn*, **70**, 2005 (1997).

5 H. Kobayashi, A. Kobayashi, and P. Cassoux, *Chem. Soc. Rev.*, **29**, 325 (2000).

6 M. Kurmoo, P. Day, P. Guionneau, G. Bravic, D. Chasseau, L. Ducasse, M. L. Allan, I. D. Marsden, and R. H. Friend, *Inorg. Chem.*, **35**, 4719 (1996).

7 I. R. Marsden, M. L. Allan, R. H. Friend, M. Kurmoo, D. Kanazawa, P. Day, G. Bravic, D. Chasseau, L. Ducasse, and W. Hayes, *Phys. Rev.*, **B50**, 2118 (1994).

8 T. Enoki, M. Enomoto, M. Enomoto, K. Yamaguchi, N. Yoneyama, J. Yamaura, A. Miyazaki, and G. Saito, *Mol. Cryst. Liq. Cryst.*, **285**, 19 (1996).

9 T. Enoki, T. Umeyama, M. Enomoto, J.-I. Yamaura, K. Yamaguchi, A. Miyazaki, E. Ogura, Y. Kuwatani, M. Iyoda, and K. Kikuchi, *Synth. Met.*, **103**, 2275 (1999).

10 A. Miyazaki, T. Umeyama, T. Enoki, E. Ogura, Y. Kuwatani, M. Iyoda, H. Nishikawa, I. Ikemoto, and K. Kikuchi, *Mol. Cryst. Liq. Cryst.*, **334**, 379 (1999).

11 A. Otsuka and G. Saito, *Synth. Met.*, **27**, B575 (1988).

12 A. Otsuka, H. Yamochi, G. Saito, T. Sugano, M. Kinoshita, S. Sato, K. Honda, K. Ohfuchi, and M. Konno, *Synth. Met.*, **41**-**43**, 1699 (1991).

13 T. Mori, A. Kobayashi, Y. Sasaki, H. Kobayashi, G. Saito, and H. Inokuchi, *Bull. Chem. Soc. Jpn.*, **57**, 627 (1984).

14 P. Wu, T. Mori, T. Enoki, K. Imaeda, G. Saito, and H. Inokuchi, *Bull. Chem. Soc. Jpn.*, **59**, 127 (1986).

15 K. Imaeda, T. Enoki, T. Mori, P. Wu, M. Kobayashi, G. Saito, and H. Inokuchi, *Synth. Met.*, **19**, 721 (1987).

16 M. Enomoto, A. Miyazaki, and T. Enoki, *Mol. Cryst. Liq. Cryst.*, **335**, 293 (1999).

17 M. Enomoto, A. Miyazaki, and T. Enoki, *Synth. Met.*, in press, (2001).

18 H. Tanaka, F. Tsuruoka, T. Ishii, H. Izumi, K. Iio, and K. Nagata, *J. Phys. Soc. Jpn.*, **55**, 2369 (1986).

19 T. Tonegawa and I. Harada, *Physica*, **B155**, 379 (1989).

20 A. Ootsuka, G. Saito, K. Ohfuchi, and M. Konno, *Phosphorus*, *Sulfur*, and *Silicon*, **67**, 333 (1992).

21 G. M. Sheldrick, "SHELXS97, Program for Crystal Structure Determination," Univ. of Göttingen, Federal Republic of Germany (1997).

22 G. M. Sheldrick, "SHELXL97, Program for Refinement of Crystal Structures," Univ. of Göttingen, Federal Republic of Germany (1997).

23 A. Bondi, *J. Phys. Chem.*, **68**, 441 (1964).

24 M. Enomoto, A. Miyazaki, and T. Enoki, to be published.

25 S. Pati, R Chitra, D. Sen, S Ramasesha, and H. R. Krishnamurthy, *J. Phys.: Condens. Matter*, **9**, 219 (1997).

26 S. Rao and D Sen, *J. Phys.: Condens. Matter*, **9**, 1831 (1997).

27 I. Yamamoto, K. Iio, and K. Nagata, *J. Phys. Soc. Jpn.*, **49**, 1756 (1980).